

# Edge Nonlinear Optics on a MoS<sub>2</sub> Atomic Monolayer

Xiaobo Yin,<sup>1,2\*</sup> Ziliang Ye,<sup>1\*</sup> Daniel A. Chenet,<sup>3\*</sup> Yu Ye,<sup>1\*</sup> Kevin O'Brien,<sup>1</sup> James C. Hone,<sup>3</sup> Xiang Zhang<sup>1,2†</sup>

The translational symmetry breaking of a crystal at its surface may form two-dimensional (2D) electronic states. We observed one-dimensional nonlinear optical edge states of a single atomic membrane of molybdenum disulfide (MoS<sub>2</sub>), a transition metal dichalcogenide. The electronic structure changes at the edges of the 2D crystal result in strong resonant nonlinear optical susceptibilities, allowing direct optical imaging of the atomic edges and boundaries of a 2D material. Using the symmetry of the nonlinear optical responses, we developed a nonlinear optical imaging technique that allows rapid and all-optical determination of the crystal orientations of the 2D material at a large scale. Our technique provides a route toward understanding and making use of the emerging 2D materials and devices.

The structural discontinuity at the edges and boundaries of 2D atomic materials, such as graphene and transition metal dichalcogenides, leads to complex interplay between the atomic positions and the electronic structures. Subsequently, the atomic edges and boundaries reconstruct structurally and electronically. A broad range of exceptional physical behaviors and applications including widely tunable transport gaps (1, 2), unusual magnetic responses (3–5), and high-performance nanoelectronics (6, 7) have been discovered. However, experimental observations of these 1D structures have been limited to scanning tunneling microscopy and transmission electron microscopy. Here, we studied the second-order

nonlinear optics on the 1D edges and boundaries of hexagonal molybdenum disulfide (MoS<sub>2</sub>) atomic membranes. The broken inversion symmetry of the atomically thin monolayer shows strong second-harmonic generation (SHG), in contrast to the centrosymmetric bulk material, which is immune to the second-order nonlinear processes. The destructive interference and annihilation of nonlinear waves from neighboring atomic membranes reveals the few-atom-wide line defects that stitch different crystal grains together, and also allows the mapping of crystal grains and grain boundaries over large areas. Our optical imaging technique enables the nonlinear optical detection of the edge states at the atomic edges of 2D crystals where the translational symmetry is broken. The observed edge resonance of SHG clearly indicates the electronic structure variation at the atomic edges, which have long been suspected to be the active sites for electrocatalytic hydrogen evolution (8).

Unlike gapless graphene, the monolayer form of transition metal dichalcogenides such as MoS<sub>2</sub> shows a direct band gap at visible frequencies, making them emergent semiconductors for nano-

electronics and optoelectronics involving photovoltaic and/or photoemission processes (9, 10). In MoS<sub>2</sub>, the unique local orbital properties of the heavy transition metal atoms and broken inversion symmetry of the monolayer crystal introduce an imbalanced charge carrier distribution in momentum space, giving rise to a novel valley-specific circular dichroism (11–12, 13). Hexagonal bulk MoS<sub>2</sub> has a layered structure with a single layer of molybdenum atoms sandwiched between two layers of sulfur atoms in a trigonal prismatic lattice. Each unit cell is formed by two mirrored sublattices, making the bulk crystal centrosymmetric and prohibiting the second-order nonlinear optical processes therein. However, in a monolayer consisting of one layer of molybdenum atoms and two sulfur atom layers, or few-layer MoS<sub>2</sub> with odd-numbered layers, the inversion center is removed, resulting in a strong second-order nonlinear optical response. The origins of the strong nonlinear optical responses and their symmetry properties have been discussed (14–16). The observed oscillatory nonlinearity between the odd-numbered and even-numbered layers is unique to all layered transition metal dichalcogenides, including MoS<sub>2</sub> and WSe<sub>2</sub> (17).

Because SHG is strongly affected by the lowered symmetry of a material, the structure and symmetry properties of MoS<sub>2</sub> atomic membranes can be probed by second-harmonic emission, which allows us to demonstrate the nonlinear optical properties of these 2D materials. Figure 1 shows the linear and nonlinear optical images of a continuous monolayer MoS<sub>2</sub> membrane epitaxially grown by chemical vapor deposition (CVD) (18). Oxide-on-silicon substrates with oxide films 285 nm thick were used for optimized optical contrast. The monolayer samples show high-quality photoluminescence and are optically uniform over large areas (Fig. 1A). In contrast, the SHG image (Fig. 1B) reveals the polycrystalline nature of the uniform monolayer, and the average grain size ranges from 20 to 40 μm. Here, the incident polarization of the pump beam is along the *y* axis and the total second-harmonic radiation is collected. The uniform SHG intensity within each grain indicates that the individual grains

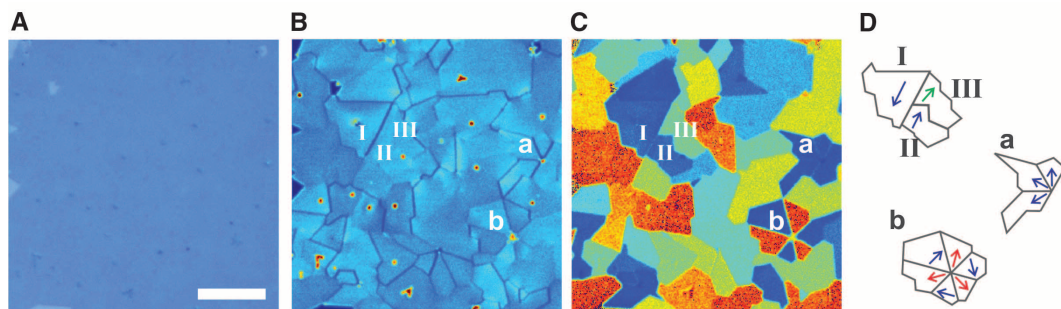
<sup>1</sup>NSF Nanoscale Science and Engineering Center, University of California, Berkeley, CA 94720, USA. <sup>2</sup>Materials Sciences Division, Lawrence Berkeley National Laboratory, Berkeley, CA 94720, USA. <sup>3</sup>Department of Mechanical Engineering, Columbia University, New York, NY 10027, USA.

\*These authors contributed equally to this work.

†Present address: Department of Mechanical Engineering, Materials Science and Engineering, University of Colorado, Boulder, CO 80309, USA.

‡Corresponding author. E-mail: xiang@berkeley.edu

**Fig. 1. All-optical determination of the crystal orientations of MoS<sub>2</sub> atomic membranes.** (A) Optical image of a large area of CVD-grown monolayer MoS<sub>2</sub>. (B) SHG image of a polycrystalline monolayer of MoS<sub>2</sub> of the same area. The grains and grain boundaries are clearly revealed by the reduced SHG intensity at the boundaries. The crystals are connected by faceted, abrupt grain boundaries. The scattered bright spots are from the nanocrystals produced in the vapor growth process. The average monolayer crystal sizes are between 20 and 50 μm. (C) The direct crystal orientation image shows the crystal orientations of the irregular-shaped polycrystalline aggregates. (D) Schematics show the flakes I and II are two crystals with



opposite orientations, as they have the same contrast in crystal orientation maps but a strongly destructive interference boundary. Crystals II and III show an orientation mismatch of ~12°. The crystal groups *a* and *b* show two cyclic twin boundaries with 60° (*a*) and 30° (*b*), respectively. Scale bar, 40 μm.

are single crystals. At the grain boundaries, however, the SHG is substantially suppressed as a result of the destructive interference and annihilation of the nonlinear waves generated from the neighboring grains with different orientations. Although the grain boundaries are only a few atom sites in width, the crystal boundaries are clearly seen. Moreover, the nonlinear generation not only reveals the symmetry properties of the crystal, but also allows the rapid mapping of crystal orientations. By analyzing the polarized components of the SHG (see supplementary text and fig. S1), we can map the crystal orientation of the polycrystalline atomic membrane. This approach allows us to capture a complete map of the crystal grain structures, color-coded according to crystal orientation (Fig. 1C). Large-area CVD-grown films clearly have complex grain geometries and orientations.

Because of the threefold rotation symmetry of monolayer MoS<sub>2</sub>, the SHG imaging without phase information does not discriminate between opposite crystal orientations. Consequently, it

only determines grain rotations modulo 60°, and the measurable difference between grain orientations is from 0° to 30°. For example, crystals I and II have no contrast in the color-coded orientation maps (Fig. 1C), but the clearly visible grain boundary between them (Fig. 1B) indicates that the two crystal grains are in opposite orientations. On the other hand, the grain boundary between crystals II and III has much less contrast (Fig. 1B), but the two crystals are distinctive when looking at the crystal orientations in Fig. 1C (~12° difference in orientation). The images obtained clearly show the twin grain structures and the sixfold symmetric patterns (Fig. 1, B and C): Crystals in group *a* have a cyclic twin structure, whereas each crystal in group *b* instead has a ~30° difference in orientation with respect to its neighbors. Such a characterization process conventionally requires diffraction-filtered dark-field transmission electron microscopy as well as a sophisticated and time-consuming analysis procedure (19). Thus, we can directly visualize the grain structure, providing key information for optimiz-

ing synthesis strategies for large-area CVD growth. The crystal orientations determined by our nonlinear optical method correspond well to transmission electron microscopy observations on the same sample. Although the results shown here were obtained for a fundamental wavelength of 1300 nm, the symmetry and the polar patterns of SHG are ubiquitous for all pump wavelengths.

Nonlinear optical susceptibilities are highly sensitive to extremely small changes in materials' electronic properties. In a 3D crystal, breaking the translational symmetry at an interface yields appreciable electric dipolar contributions to the surface optical nonlinearity, making the highly surface- and molecular-specific second-harmonic spectroscopy an indispensable tool for noninvasive study of surface sciences (20). Not only does it measure dipolar width across interfaces (21), it also probes the real-time dynamics of a surface, such as atomic reconstructions, charge transfer, and molecular conformational transitions. We found that the broken translational symmetry at the edge of a 2D crystal potentially creates 1D atomic edges with localized electronic properties that may substantially differ from the 2D bulk. Shown in Fig. 2, A and B, are SHG images of discrete triangular CVD-grown monolayer islands at pump wavelengths of 1280 nm and 1300 nm, respectively. Although actually rough at the atomic scale, the edges of these monolayer islands are the more energetically favorable termination of molybdenum zigzag edges, and they appear straight and sharp under the optical microscope (18). The SHG images with two different fundamental wavelengths differ at these atomic edges. When pumped at 1300 nm, a brim of enhanced SHG is observed at the edges of the crystals (Fig. 2B), which is substantially stronger than that of the central region. At the corners, the SHG is even stronger. By comparison, no such enhancement is observed at the edges at the pump wavelength of 1280 nm. The edge-enhanced SHG is further seen in the cross sections in Fig. 2C. Structure and field discontinuities at the edges of these 2D crystals can potentially lead to enhanced in-plane nonlinear polarizability, like the surface-enhanced SHG often observed on metal and dielectric surfaces (22, 23). Such enhancement, however, is equally effective for different pump wavelengths as long as there are no additional electronic states located at the edge. The stronger second-harmonic edge responses pumped at 1300 nm versus 1280 nm are therefore the results of the electronic structure variations between the sharp crystalline edges and the bulk monolayer crystals. Moreover, assuming that the region where the electronic states are affected by the existence of the atomic edges is about the same as the thickness (i.e., less than 1 nm), it requires more than three orders of magnitude of nonlinear enhancement to exceed the nonlinear generation in the central region, given an illumination pump laser spot size greater than 1 μm.

To further probe these phenomena, we imaged the SHG at the edges and corners of the

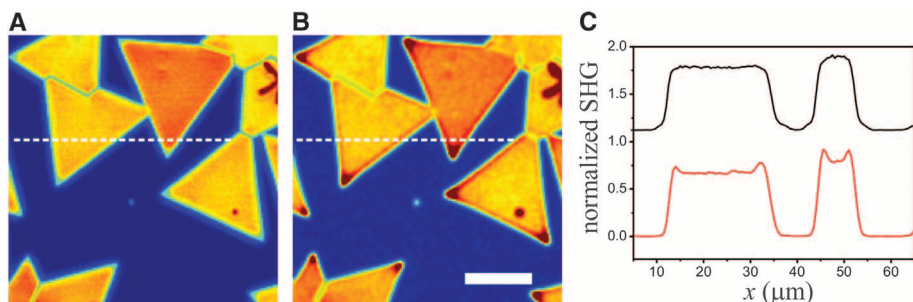


**Fig. 2. SHG image of discrete triangular islands of MoS<sub>2</sub> crystals.** (A) SHG image pumped at 1280 nm. (B) SHG image of the same sample pumped at 1300 nm. The brim of crystal shows a strong nonlinear optical (SHG) edge state. Scale bar, 20 μm. (C) Cross sections [white dashed lines in (A) and (B)] compare the SHG of the same crystal under pump wavelengths of 1280 nm (black) and 1300 nm (red), respectively. The enhanced edge responses are clearly shown.

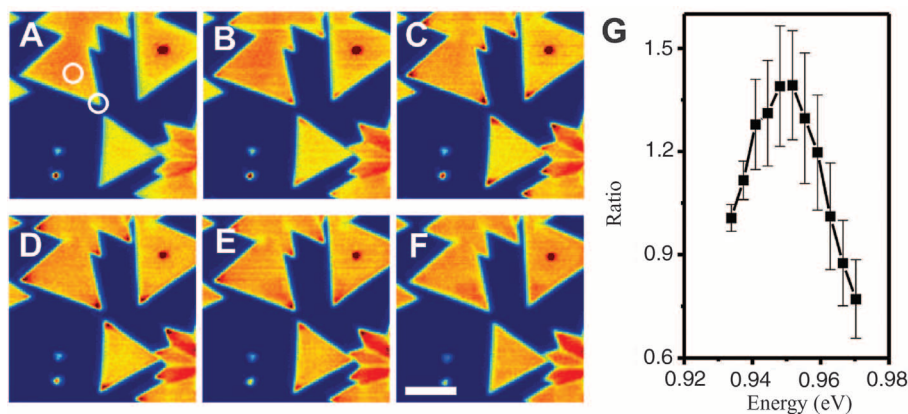
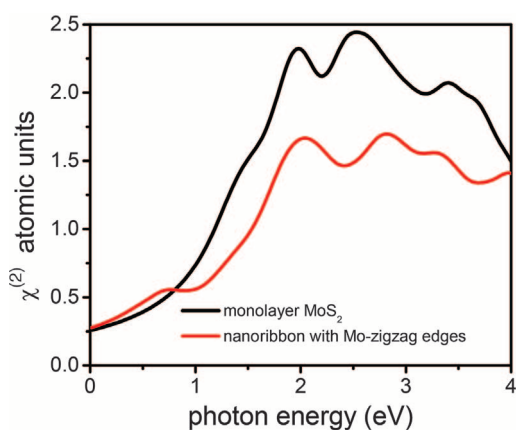


**Fig. 3. Nonlinear edge resonance of MoS<sub>2</sub> monolayer membrane.** (A to F) SHG images of the same monolayer MoS<sub>2</sub> sample for fundamental wavelengths of 1280 nm, 1290 nm, 1300 nm, 1310 nm, 1320 nm, and 1330 nm, respectively. Scale bar, 20 μm. (G) Resonance of the edge nonlinear response at ~0.947 eV (1310 nm). The ratio is determined by the integrated SHG with the areas circled in (A).

**Fig. 4. Dispersion of the nonlinear permittivity for both the monolayer MoS<sub>2</sub> and the nanoribbon with Mo-zigzag edges derived from DFT.** The monolayer (black) shows no spectroscopic features (dispersive and lossless) at the low photon energies, and the features between 1.5 and 4.0 eV are associated with interference between the one-photon and two-photon processes. The nanoribbon (red) shows a two-photon resonance at the photon energy ~0.8 eV due to the subband transitions from the valence bands to the isolated edge states originating from the Mo-zigzag edges. The nanoribbon considered here has a width of 5 unit cells, and both the edges are terminated by Mo-zigzag edges. The lattice constants were assumed to be the same as the monolayer, and the Mo edges are not passivated for simplicity. The overall nonlinear responses are averaged over the entire supercell that includes both the nanoribbon and the vacuum; the enhancement of nonlinear responses could therefore be severely underestimated.



samples at different fundamental wavelengths. We observed a resonance wavelength is about 1310 nm (~0.95 eV), a slightly higher photon energy than the half transition energy of the *A* exciton complex (Fig. 3). Quantum mechanical expression for the second-order nonlinear susceptibility of a material involves matrix elements with one occupied and two unoccupied intermediate states. When there are additional energy levels nearly coincident with virtual transition levels, the coupling between the radiation and the nonlinear optical susceptibility becomes large. The nonlinear optical transition matrix elements at the edges may involve additional occupied edge states relative to the crystalline atomic membrane, resulting in strongly enhanced second-order nonlinear susceptibilities. Density functional theory (DFT) has predicted the existence of these edge states and provides atomic-scale insight into them (24); such 1D edges have been identified on nanoparticulate MoS<sub>2</sub> clusters on single-crystal gold by scanning tunneling microscopy in ultrahigh vacuum (25). The existence of special electronic edge states for finite low-dimensional crystals has also been reported in graphene nanoribbons (26, 27) and at the end of 1D atomic chains (end states) (28). We observed the strong optical nonlinear responses of such edges in 2D MoS<sub>2</sub> membranes, which have been suspected to be the active sites for electrocatalytic hydrogen evolution (8). As a control experiment, there are no extraordinary photoluminescence responses observed on these edges (fig. S6). It is also worth noting that there exist prominent excitons in thin-film MoS<sub>2</sub> (29) and that strongly correlated excitons, especially those with high binding energies, can potentially have an impact on second-order nonlinearities. Moreover, the local doping profile at the boundaries and edges introduced during the growth may also account for the difference at the edges and the center of the monolayer crystals.

The linear and nonlinear optical properties of monolayer MoS<sub>2</sub> can be investigated with first-

principles calculations (see supplementary text). The probabilities of virtual electronic transitions can be derived from second-order perturbation theory (30). As shown in Fig. 4, we have calculated the dispersion of the nonlinear optical susceptibilities using the full potential linear augmented plane wave method within DFT. Because MoS<sub>2</sub> belongs to the point group *D*<sub>3h</sub>, there is only one independent component, namely  $\chi^{(2)} = \chi_{xyx}^{(2)} = \chi_{yxx}^{(2)} = \chi_{yxx}^{(2)} = \chi_{yyx}^{(2)}$ . In Fig. 4, the tensor elements  $\chi^{(2)}$  of monolayer MoS<sub>2</sub> and of a nanoribbon with zigzag Mo termination are compared. The monolayer shows no spectroscopic features below the band gap (~1.9 eV). In stark contrast, the zigzag nanoribbon shows a two-photon resonance at ~0.8 eV, originating from the subband transitions from the valence bands to the isolated edge states of the Mo-zigzag edges. Such a two-photon nonlinear optical resonance qualitatively explains the experimental observations at 1300 nm. In our calculations, we considered an infinitely long nanoribbon with a width of five unit cells with Mo-zigzag edge terminations. The lattice constants are assumed to be the same as the monolayer, and the Mo edges are not passivated for simplicity. The overall nonlinear responses are averaged over the entire supercell that includes both the vacuum and the nanoribbon. Therefore, the enhancement of nonlinear responses near 0.8 eV could be severely underestimated. The spectroscopic features between 1 and 4 eV are mainly associated with interference between the one-photon and two-photon processes, which are commonly observed in nonlinear semiconductors.

Our technique has revealed second-order nonlinear optics at the boundaries and edges of the atomic membranes of the hexagonal transition metal dichalcogenide MoS<sub>2</sub>, with the strong optical resonance indicating a distinct edge state due to the translational symmetry breaking. The nonlinear response reveals the structural and symmetry information of the 2D atomic monolayer based on interference of nonlinear waves. Such a

rapid nonlinear optical imaging technique will allow exploration of the structural, optical, and electronic properties of 2D atomic layers over a large area.

## References and Notes

1. Y. W. Son, M. L. Cohen, S. G. Louie, *Phys. Rev. Lett.* **97**, 216803 (2006).
2. X. Li, X. Wang, L. Zhang, S. Lee, H. Dai, *Science* **319**, 1229–1232 (2008).
3. O. V. Yazyev, M. I. Katsnelson, *Phys. Rev. Lett.* **100**, 047209 (2008).
4. M. Sepioni *et al.*, *Phys. Rev. Lett.* **105**, 207205 (2010).
5. O. V. Yazyev, *Rep. Prog. Phys.* **73**, 056501 (2010).
6. O. V. Yazyev, S. G. Louie, *Nat. Mater.* **9**, 806–809 (2010).
7. A. W. Tsen *et al.*, *Science* **336**, 1143–1146 (2012).
8. T. F. Jaramillo *et al.*, *Science* **317**, 100–102 (2007).
9. B. Radisavljevic, A. Radenovic, J. Brivio, V. Giacometti, A. Kis, *Nat. Nanotechnol.* **6**, 147–150 (2011).
10. A. Splendiani *et al.*, *Nano Lett.* **10**, 1271–1275 (2010).
11. T. Cao *et al.*, *Nat. Commun.* **3**, 887 (2012).
12. H. Zeng, J. Dai, W. Yao, D. Xiao, X. Cui, *Nat. Nanotechnol.* **7**, 490–493 (2012).
13. K. F. Mak, K. He, J. Shan, T. F. Heinz, *Nat. Nanotechnol.* **7**, 494–498 (2012).
14. L. M. Malard, T. V. Alencar, A. P. M. Barboza, K. F. Mak, A. M. de Paula, *Phys. Rev. B* **87**, 201401R (2013).
15. N. Kumar, Q. Cui, F. Ceballos, H. Zhao, *Phys. Rev. B* **87**, 161403 (2013).
16. Y. Li *et al.*, *Nano Lett.* **13**, 3329–3333 (2013).
17. H. Zeng *et al.*, *Sci. Rep.* **3**, 1608 (2013).
18. A. M. van der Zande *et al.*, *Nat. Mater.* **12**, 554–561 (2013).
19. P. Y. Huang *et al.*, *Nature* **469**, 389–392 (2011).
20. Y. R. Shen, *Nature* **337**, 519–525 (1989).
21. W. H. Steel, R. A. Walker, *Nature* **424**, 296–299 (2003).
22. N. Bloembergen, P. S. Pershan, *Phys. Rev.* **128**, 606–622 (1962).
23. C. K. Chen, A. R. B. de Castro, Y. R. Shen, *Phys. Rev. Lett.* **46**, 145–148 (1981).
24. M. V. BOLLINGER *et al.*, *Phys. Rev. Lett.* **87**, 196803 (2001).
25. S. Helveg *et al.*, *Phys. Rev. Lett.* **84**, 951–954 (2000).
26. K. Nakada, M. Fujita, G. Dresselhaus, M. S. Dresselhaus, *Phys. Rev. B* **54**, 17954–17961 (1996).
27. C. G. Tao *et al.*, *Nat. Phys.* **7**, 616–620 (2011).
28. J. N. Crain, D. T. Pierce, *Science* **307**, 703–706 (2005).
29. K. F. Mak *et al.*, *Nat. Mater.* **12**, 207–211 (2013).
30. J. E. Sipe, D. J. Moss, H. M. Vandriel, *Phys. Rev. B* **35**, 1129–1141 (1987).

**Acknowledgments:** Supported by the U.S. Air Force Office of Scientific Research, Multidisciplinary University Research Initiative program, under grant FA9550-12-1-0024. The synthesis of the material was supported by the Center for Re-Defining Photovoltaic Efficiency Through Molecular-Scale Control, an Energy Frontier Research Center funded by the U.S. Department of Energy, Office of Science, Office of Basic Energy Sciences under award DE-SC0001085 (D.A.C. and J.C.H.).

## Supplementary Materials

www.sciencemag.org/content/344/6183/488/suppl/DC1  
Supplementary Text  
Figs. S1 to S6  
References (31–40)

8 January 2014; accepted 11 March 2014  
10.1126/science.1250564

---

*This copy is for your personal, non-commercial use only.*

---

**If you wish to distribute this article to others**, you can order high-quality copies for your colleagues, clients, or customers by [clicking here](#).

**Permission to republish or repurpose articles or portions of articles** can be obtained by following the guidelines [here](#).

**The following resources related to this article are available online at [www.sciencemag.org](http://www.sciencemag.org) (this information is current as of June 29, 2015 ):**

**Updated information and services**, including high-resolution figures, can be found in the online version of this article at:

<http://www.sciencemag.org/content/344/6183/488.full.html>

**Supporting Online Material** can be found at:

<http://www.sciencemag.org/content/suppl/2014/04/30/344.6183.488.DC1.html>

A list of selected additional articles on the Science Web sites **related to this article** can be found at:

<http://www.sciencemag.org/content/344/6183/488.full.html#related>

This article **cites 37 articles**, 4 of which can be accessed free:

<http://www.sciencemag.org/content/344/6183/488.full.html#ref-list-1>

This article has been **cited by** 1 articles hosted by HighWire Press; see:

<http://www.sciencemag.org/content/344/6183/488.full.html#related-urls>

This article appears in the following **subject collections**:

Physics

<http://www.sciencemag.org/cgi/collection/physics>